EXPERIMENTAL MODELLING OF THE DYNAMIC BEHAVIOUR OF A SPAR BUOY WIND TURBINE

Giuseppe Roberto Tomasicchio [1], Felice D'Alessandro [1], Alberto Maria Avossa [2], Luigia Riefolo [1,3], Elena Musci [4], Francesco Ricciardelli [2], Diego Vicinanza [2]*

Abstract

This paper summarises the experience gained from wave basin experiments aimed at investigating the dynamic response of a spar buoy offshore wind turbine, under different wind and wave conditions. The tests were performed at the Danish Hydraulic Institute within the framework of the EU-Hydralab IV Integrated Infrastructure Initiative. The Froude-scaled model was subjected to regular and irregular waves, and to steady wind loads. Measurements were taken of hydrodynamics, displacements of the floating structure, wave induced forces at critical sections of the structure and at the mooring lines. First, free vibration tests were performed to obtain natural periods and damping ratios. Then, displacements, rotations, accelerations, and forces were measured under regular and irregular waves and three different wind conditions corresponding to cut-in, rated speed and cut-out. Statistical and spectral analyses were carried out to investigate the dynamic behaviour of the spar buoy wind turbine.

The results show that most of the dynamic response occurs at the wave frequency, with minor contributions at the first and second harmonics of this, and at the natural rigid-body frequencies. In addition, in many cases a non-negligible contribution was found at the first bending frequency of the structure; this suggests that Cauchy scaling of the model cannot be neglected.

According to the EU-Hydralab IV programme 'Rules and conditions' (www.hydralab.eu), the raw data are public domain, and therefore they represent a unique dataset of measurements, possibly useful for further analyses, for calibration and validation of numerical models, and for comparison with full scale observations.

Keywords: floating wind turbines; spar buoy; dynamic analyses; public datasets; hydrodynamic damping.

[1] Engineering Department, University of Salento, Campus Ecotekne, via Monteroni, 73100 Lecce, Italy. e-mail: roberto.tomasicchio@unisalento.it; felice.dalessandro@unisalento.it
[2] Department of Civil Engineering, Design, Building and Environment, University of Campania "Luigi Vanvitelli", via Roma 9, 81031 Aversa (CE), Italy. e-mail: albertomaria.avossa@unicampania.it; friccia@unicampania.it; diego.vicinanza@unicampania.it
[3] Department of Civil and Environmental Engineering, Politecnico di Milano, Piazza Leonardo da Vinci 32, 20133 Milan, Italy. e-mail: luigia.riefolo@polimi.it
[4] Autorità Idrica Pugliese Bari, Italy. e-mail: elena.musci@alice.it

[*]*Corresponding author*

1. INTRODUCTION

In the last years, energy consumption has enormously increased worldwide. In this context, the European Union has set the goal of producing 22.1% of energy from renewable sources by 2020, in accordance with the Kyoto protocol. With the ambitious COP21 agreement, more nations will start down a path towards renewable energy production, as a pledge towards climate policies. This increased demand for renewable energy production has triggered a large amount of research on coastal and offshore devices, able to produce energy from waves, currents, and wind.

The vision for large scale offshore floating Wind Turbines (WTs) was introduced by Heronemus in 1972 [1], but it was not until the mid 1990s, after the commercial wind industry was well established, that the topic was taken up again by the mainstream research community [2]. While the fixed WT technology can be considered mature, and many turbines have been installed in water depths up to around 25 m, it is recognized that to reach the objectives of renewable energy production it will be necessary to expand the technology for deeper waters, adopting a floater as support structure for offshore WTs.

An offshore WT can use different floating system configurations. In fact, there is a large variety of floater geometries, of mooring systems and of ballast options used in the offshore oil and gas industry, which can be readily adapted by the wind energy industry. With particular reference to platforms, these can be classified based on how they achieve stability in pitch and roll. Currently, there are two main categories of offshore floating WT platform concepts, the Tension Leg Platform (TLP) type and the Spar Buoy (SB) type.

The TLP is made of a floating platform with lines tethered from its corners to concrete blocks or other mooring systems lying at the sea bottom. On the other hand, the SB is made of a long vertical floating cylinder having approximately half of its length underwater; the cylinder is ballasted in its lower part, which provides dynamic stability to the system. The SB is usually kept in position by a catenary spread mooring system using anchor-chains, steel cables and/or synthetic fibre ropes (Figure 1).

However, although the interest of the scientific community for floating offshore WTs is developing quickly, the dynamic behaviour of these structures under wave and wind actions still remains an unsolved and complex issue, and a challenge in offshore engineering.

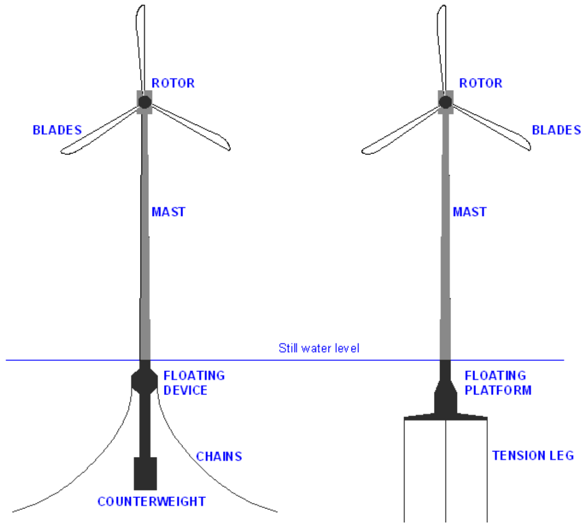

Figure 1. Spar buoy (SB), left, and tension leg platform (TLP), right, floating WTs.

From a hydrodynamic point of view, wave-structure interaction is bi-directional, i.e. the structure responds to viscous loads generated by the fluid flow, and to the linear diffraction; at the same time it produces eddies, currents, and wakes, which interact with the incident wave field. In addition, offshore structures are exposed to higher waves than coastal structures, as well as to the complexities of short-crested sea waves in combination with stronger winds, gust bumps, wind-induced broken waves (i.e. white capping and steeper waves) and intense currents. Furthermore, slender cylindrical bodies are known to be subjected to vortex-induced motions [3, 4], possibly inducing large-amplitude lateral displacements caused by synchronization phenomena. In addition, the analysis and design of offshore WTs are made more even complicated by the presence of the rotor and by the action of the mooring lines [5]. Linear and higher-order diffraction and radiation forces, together with the nonlinear Morison's type quadratic hydrodynamic drag loading imposed to the floating body, and with the nonlinear response of the mooring lines, gives rise to a highly complex coupled dynamic system.

For the above reasons, evaluation of the design loads and expected dynamic response of offshore floating WTs becomes a very complex topic, involving coupled wave and wind models, multivariate probability analysis [6-8] and advanced load calculation methods [9-11]. To date, only a limited number of studies is available on the dynamic response of floating offshore WTs [12-17], and the broad interest in renewable energies has increased the demand of quality tests, to optimize the design of innovative floating offshore WTs and to collect reliable and accurate data for further calibration and verification of numerical models [18].

Previous experimental investigations allowed gaining information on flow characteristics around structures and flow-induced forces [16, 19-21]. Physical observations can give a paramount contribution toward the rational definition of wave-structure interaction [22-24]. Therefore, the working features of floating offshore WTs needs being investigated through large-scale offshore engineering laboratory experiments. In the past, the results of these have been subjected to disclosure restrictions and confidentiality issues.

This paper describes some of the experience gained from physical model experiments aimed at investigating the dynamic response of two different floating offshore WT technologies, the TLP and SB, under different wind and wave conditions, and at overcoming the limitations in the available public domain dataset. In the tests two prototypes, a TLP and a SB were taken as reference, the MIT/NREL [5, 25] and the OC3-Hywind [12, 26].

The objectives of the research activity have been mainly oriented at: (*a*) exploring the feasibility of wave-basin experiments on floating WTs, and pointing out the major difficulties; (*b*) gaining basic knowledge of the hydrodynamic and dynamic behaviour of floating wind turbines; (*c*) investigating the interaction between the mooring lines and the floating body; (*d*) create a reliable database for numerical modelling calibration and verification; (*e*) create a reliable database for comparison with full scale measurements.

For the sake of brevity, the results presented in this paper are limited to the SB case. The TLP case will be considered in a future paper, which will include a comparison between the TLP and SB behaviour under the same wind and wave conditions. According to the EU-Hydralab IV programme 'Rules and conditions' (www.hydralab.eu), the raw data used for this paper are public domain.

2. SPAR BUOY PHYSICAL MODEL AND SETUP

The SB physical model was designed with reference to the OC3-Hywind prototype [12, 26]. The OC3-Hywind is a SB floating WT developed within the Offshore Code Comparison Collaboration (OC3), a project operating under Subtask 2 of the International Energy Agency (IEA) Wind Task 23.1. The OC3-Hywind system resembles the Hywind concept developed by Statoil Hydro in Norway; it features a 120 m, deeply drafted slender SB, with three catenaries mooring lines. The lines are attach to the platform by a delta connection (or "crowfoot"), to increase the yaw stiffness of the mooring system. The length scale of the Froude-scaled model is 1:40. Tables 1 and 2 summarize the geometric and dynamic properties of the prototype and model OC3-Hywind SB (Figure 2).

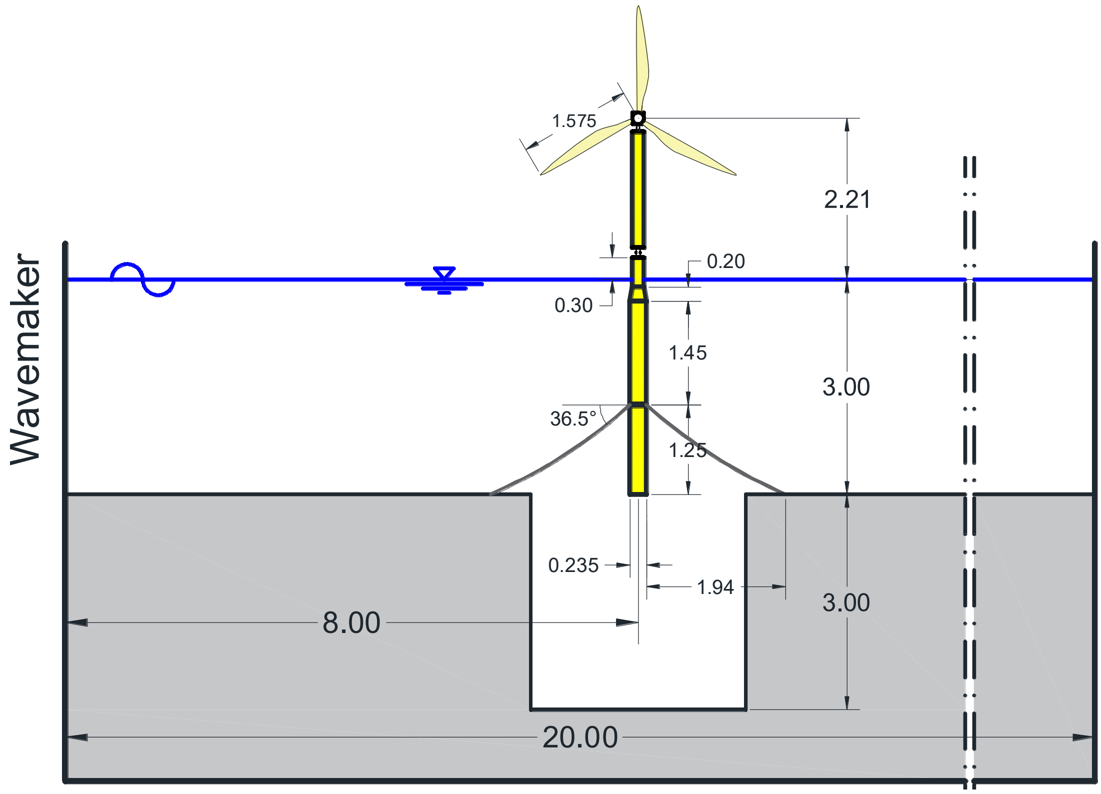

Figure 2. Sketch of the SB model in the wave basin.

2.1 Floater characteristics

The floater of the SB model was designed consisting of five main parts, from top to bottom: (*a*) an upper cylinder, 1810 mm long with an outer diameter of 162.5 mm; (*b*) a 140 mm long connection element for hosting load cells, (*c*) an intermediate cylinder, 400 mm long with an outer diameter of 162.5 mm, (*d*) 200 mm long cone with an upper diameter of 162.5 mm and a lower diameter of 235 mm, and (*e*) a 2700 mm long cylinder with a diameter of 235 mm. The lower cylinder has a removable bottom 100 mm long, which was used to place the ballast. During the tests, the still water level (SWL) was 300 mm below the top of the intermediate cylinder. Ballast was designed to match scale requirements; lead bars and small lead spheres with a total weight of 92.5 kg were inserted at the bottom of the SB; a foam cover prevented the spheres from moving during testing. Figure 3 shows a photo of the setup of the floating SB.

Table 1. Geometric characteristics of the SB OC3-Hywind. Length scale λ = 1:40.

SB OC3-HYWIND	Full scale	Unit	Scale factor	Scaled model
SB diameter above taper	6.50	m	λ	0.162
SB diameter below taper	9.40	m	λ	0.235
Depth to top of taper below SWL	4.00	m	λ	0.100
Depth to bottom of taper below SWL	12	m	λ	0.300
Depth to floater base below SWL (total draft)	120	m	λ	3.000
Tower height	88.50	m	λ	2.212
Hub level	90	m	λ	2.250
Hub diameter	3.00	m	λ	0.075
Radius to fairleads	9.40	m	λ	0.235
Radius to anchors	9.40	m	λ	0.235
Depth to fairleads	70	m	λ	1.750
Depth to anchors	320	m	λ	8.000
Depth of C.o.M. below SWL	89.92	m	λ	2.248
Unstreached line length	902	m	λ	22.56
Line diameter	90	mm	λ	2.25
Angle between adjacent lines	120	Deg.	λ^0	120

Table 2. Dynamic properties of the SB OC3-Hywind. Length scale λ = 1:40.

SB OC3-HYWIND	Full scale	Unit	Scale factor	Scaled model
Rotor mass	110,000	kg	λ^3	1.677
Nacelle mass	240,000	kg	λ^3	3.658
Tower mass	347,500	kg	λ^3	5.297
Floating system mass (including ballast)	7,466,330	kg	λ^3	113.82
Total mass	8,163,830	kg	λ^3	124.45
Water displacement	8,029	m^3	λ^3	0.125
Buoyancy (water displacement x sea water density)	8,229,725	kg	λ^3	125.45
Buoyancy - Total Mass	65,895	kg	λ^3	1.004
Line mass density	78	kg/m	λ^2	0.0474
Suspended line = (Buoyancy – Total Mass) / (Line Mass density) / 3	283	m	λ	7.066

2.2 Mooring system design

According to Jonkman [12], the total vertical component of the force that the full-scale buoy experiences from the three mooring lines is 1,607 kN, therefore, each line applies a vertical force F_V = 535.7 kN to the SB. From the vertical component of the force, and considering that the submerged weight of the line per unit length is w = 698.1 N/m, it was possible to determine the length l_s of the suspended mooring line, assuming that this is inextensible:

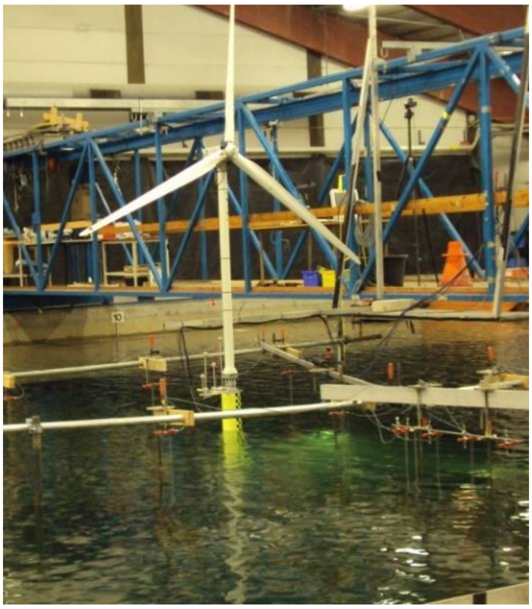

Figure 3. Spar buoy wind turbine model in the wave basin.

$$l_s = \frac{F_V}{w} = 767.3\,\text{m} \tag{1}$$

Being the vertical distance of the fairleads to the sea bottom D = 250 m, the horizontal component of the mooring force is [27]:

$$F_H = \frac{w(l_s^2 - D^2)}{2D} = 734.8\,\text{kN} \tag{2}$$

The horizontal component of the suspended mooring line length is:

$$x = \frac{F_H}{w}\cosh^{-1}\left(\frac{wD}{F_H} + 1\right) = 711.8\,\text{m} \tag{3}$$

moreover, the distance x_A of the fairlead to the anchor is:

$$x_A = l - l_s + x = 846.7\,\text{m} \tag{4}$$

l = 902.2 m being the total length of the line.

The design of the mooring system was carried out through a static analysis of one single line using STATMOOR Code [28]; this allows handling the static analysis of extensible mooring lines made of several segments, each of which having different geometric properties and with attached submerged buoys.

Inserting the value of F_H as input to STATMOOR, the static equilibrium configuration of a single mooring line was obtained, together with the vertical component of the force at the top and with the horizontal distance of the top of the line to the anchor.

The full-scale mooring system is specified to 320 m water depth, whereas the 3 m deep basin allows reaching only a corresponding full-scale depth of 120 m in a scale of 1:40. Therefore, it was necessary to distort the model by truncating the mooring lines. The designed mooring system consisted of three lines directly connected to the main cylinder using a collar with fairleads placed 1.75 m below SWL. The angle between two adjacent mooring lines was 120°. The mooring lines were truncated at a vertical distance of 1.25 m and a horizontal distance of 1.94 m from the fairleads. Each line was made of a thin rope 1.7 mm in diameter, with a weight of 2.4 g/m and an extensional stiffness of 6.25 N/mm. Force transducers having a maximum load capacity of 300 N measured the forces at the top of the three mooring lines. Between the transducers and the mooring lines, 0.75 m long springs were placed, with a stiffness of about 28.4 N/m. The mooring lines were pre-tensioned with weights of 1.5 kg each, so to reproduce the same initial configuration in terms of zenital angle (36°) and lateral force F_H at fairleads, and stiffness properties of the longer chain mooring lines.

2.3 Tower, rotor and blades

An overview of the instrumentation of the rotor and of the tower is given in Figures 4 and 5, respectively. Tables 3 and 4 summarize the properties of the WT and of the blades, respectively.

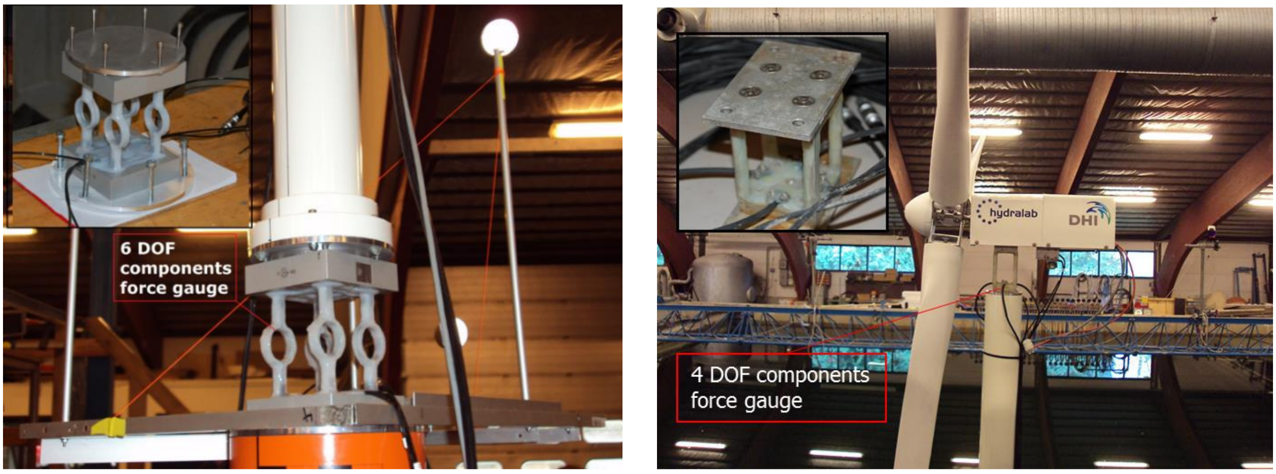

(a) (b)

Figure 4. (a) 6-DOF force gauges placed at the base of the tower. (b) Rotor, nacelle and 4-DOF force gauge placed between the tower and the nacelle.

Table 3. Summary of properties of the WT. Length scale λ = 1:40.

WT	Full scale	Unit	Scale factor	Scaled model
Rotor mass	110,000	kg	λ^3	1.677
Nacelle mass	240,000	kg	λ^3	3.658
Rated rotor speed	12.1	rpm	λ^0	12.1
Overhang	5.00	m	λ	0.125
Shaft tilt	5.0	Deg.	λ^0	5.0

Table 4. Summary of properties of the blades.

Blade	Weight [g]	Centre of gravity [cm]
1	496	42.2
2	475	41.7
3	477	42.1

A six component force gauge was mounted at the base of the tower, between the tower and the floater, measuring $F_{x,base}$, $F_{y,base}$, $F_{z,base}$ and $M_{x,base}$, $M_{y,base}$ and $M_{z,base}$. The tower was made out of a plastic cylinder, with an outer diameter of 80 mm and a length of 1615 mm. At the top of the tower, between the tower and the nacelle, a four components force gauge was mounted, measuring $F_{x,top}$, $F_{y,top}$, $M_{x,top}$ and $M_{y,top}$. Furthermore, three accelerometers were placed at different levels along the tower; in particular, two accelerometers were located underneath the nacelle, measuring the lateral (y) and vertical (z) accelerations, and a third one at the bottom of the tower, measuring the longitudinal (x) acceleration.

A motor inside the casing induced the rotation for the rotor. A potentiometer adjusted the rotational speed to 38 rpm, which corresponds to a rotational speed of 12.1 rpm full scale. This allowed for gyroscopic effects.

The rotor blades were made of fiberglass and were geometrically scaled from a real case. Each blade had a length of 1.575 m (Figure 5). The pitch of the blades was set to 30°, giving rise to a measured thrust of 3 N at 38.1 rpm, model scale. Further tests to obtain a relationship between thrust and rotational speed were carried out with rotational speeds of 32 rpm and 42 rpm, model scale.

Only static wind loads were reproduced, by applying the mean thrust force to the nacelle. This was done with a weightless line connected to the nacelle, passing through a pulley and with a suspended mass. The full-scale thrust for the 5 MW NREL reference turbine was calculated by different researchers, for example by Sclavounos *et al.* [29] who found that the rotor thrust under an 11 m/s wind is equal to about 800 kN, corresponding to 10 N for the 1:40 scaled model. Almost 3 N came from the trust force generated by the rotor, and the difference was obtained with a weight of 7 N.

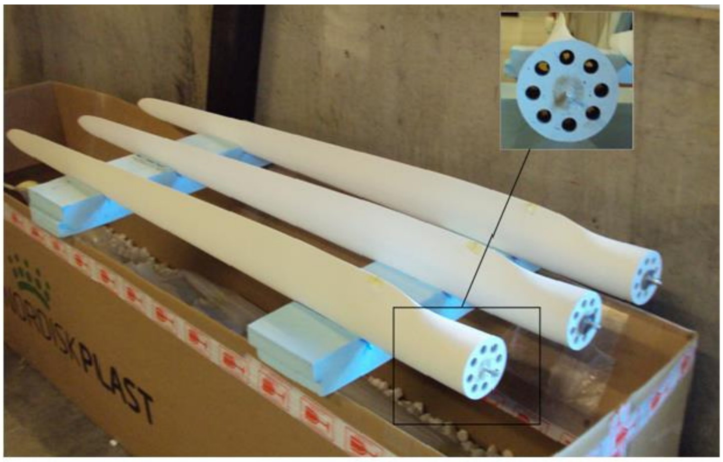

Figure 5. Blades profile and connection section.

3. WAVE GENERATION AND BASIN INSTRUMENTATION

The experiments were performed at the DHI Offshore Wave Basin in Hørsholm, Denmark. The wave basin (Figure 6) is 20 m long and 30 m wide, with a water depth of 3 m and a 6 m deep pit. The floating structure was placed at the centre of the pit, at a distance of 8 m from the wave maker, which lies on the 30 m wide side of the basin.

The wave maker is equipped with 60 individually controlled flaps, able of generating regular and irregular waves. A parabolic wave absorber located opposite to the wave maker minimized reflection. The characteristics of the incident and reflected waves were evaluated through a five wave-gauge array reflection analysis [30]. Wave calibration was made placing the five gauges at the centre of the pit; during the model tests, the gauges were moved 3 m downstream the floating structure. In addition, six wave gauges were located around the structure; an array of three was located 1.50 m upstream of the model and another array of three 1.50 m downstream the model.

A Nortek Vectrino velocimeter measured the velocity field in the proximity of the structure. The ADV was located at a distance of 60 cm from the front size of the floater. A Qualisys Track System (www.qualisys.com) tracked the six DoF rigid body motion of the model: surge, sway, heave, roll, pitch and yaw. The system is based on two cameras emitting infrared light. Five passive spherical markers, 40 mm in diameter, reflect the infrared light; these were positioned on a frame mounted at the tower base, just below the six-component force gauge. Data processed by the Qualisys Track Manager were directly transferred through an analog output to the main data acquisition system and thus synchronized with all other recorded data.

All the sensors were synchronized using the DHI Wave Synthesizer. Sampling took place at 40 Hz and lasted 3 minutes for each regular wave case and 10 minutes for each irregular wave case.

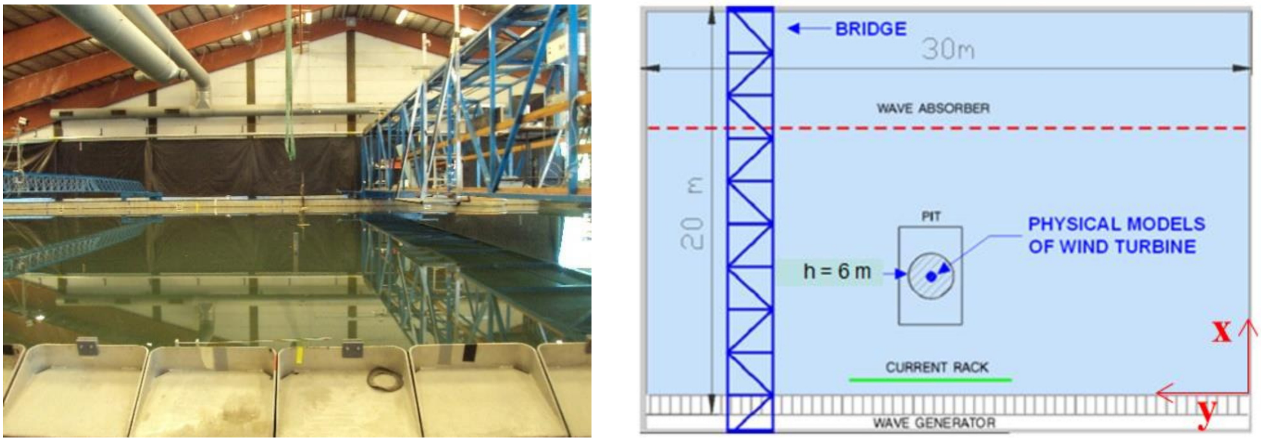

Figure 6. DHI Offshore Wave Basin in Hørsholm, Denmark.

4. TEST PROGRAM

According to IEC 61400-1 and IEC 61400-3 [31, 32], the three conditions of cut-in, of rated speed and cut-out were considered in the tests. First, cut-in conditions were tested; then, the rated speed condition was simulated, combining mean thrust, rotating rotor and different sea states with regular and irregular waves; finally, extreme wave conditions were generated, with the rotor being stopped and mean thrust corresponding to cut-out wind speed. Long-crested regular and irregular waves were generated, orthogonal (0°) and oblique (20°) to the structure. The selected wave conditions refer to typical storm conditions, for both sea and ocean areas. In Table 5 the characteristics of the generated waves are given, where H and T indicate the regular wave height and wave period, respectively, and H_s and T_p indicate the significant wave height and peak wave period, respectively.

Table 5. Test program.

Wind speed (rotor condition)	Waves	Prototype scale		Model scale	
		***H* or *H*$_s$ [m]**	***T* or *T*$_p$ [s]**	***H* or *H*$_s$ [cm]**	***T* or *T*$_p$ [s]**
0 m/s (parked) 11.4 m/s (rated)	Regular	1.00	10.1	2.5	1.6
		1.56	12.6	3.9	2.0
		1.80	15.2	4.5	2.4
		4	11.4	10	1.8
		6		15	
		8		20	
		6	12.6	15	2.0
			15.2		2.4
	Irregular	4	10.1	10	1.6
		6		15	
11.4 m/s (rated) 25 m/s (stalled)	Regular	10	11.4	25	1.8
		12	12.6	30	2.0
			15.2		2.4
	Irregular	8	12.6	20	2.0

5. RESULTS AND DISCUSSION

All data from the tests were converted to full scale using Froude scaling before being analysed. In particular, eight tests with different wave characteristics, *H* and *T,* and rotor blades conditions (parked/operational) were selected for discussion (Table 6). For all the selected tests, wave incidence was orthogonal to the structure.

Table 6. Regular wave tests considering in the discussion.

H **[m]**	***T*** **[s]**	**Parked**	**Rated**	**Stalled**
4	11.4	1380	1414	-
6	11.4	1381	1415	-
8	11.4	1382	1416	-
10	11.4	-	1481	1443

5.1 Free decay tests

Free decay tests were carried out to evaluate the surge, sway, roll and pitch natural frequencies and damping ratios of the SB wind turbine. Figure 7 shows the normalized Power Spectral Density Functions (PSDFs) $f \cdot S(f)/\sigma^2$ of the non-stationary measured surge, sway, pitch and roll, evaluated by MATLAB®. Natural frequencies of 0.011 Hz were found for the surge and sway motions and of 0.024 Hz for the roll and pitch motions (Table 7).

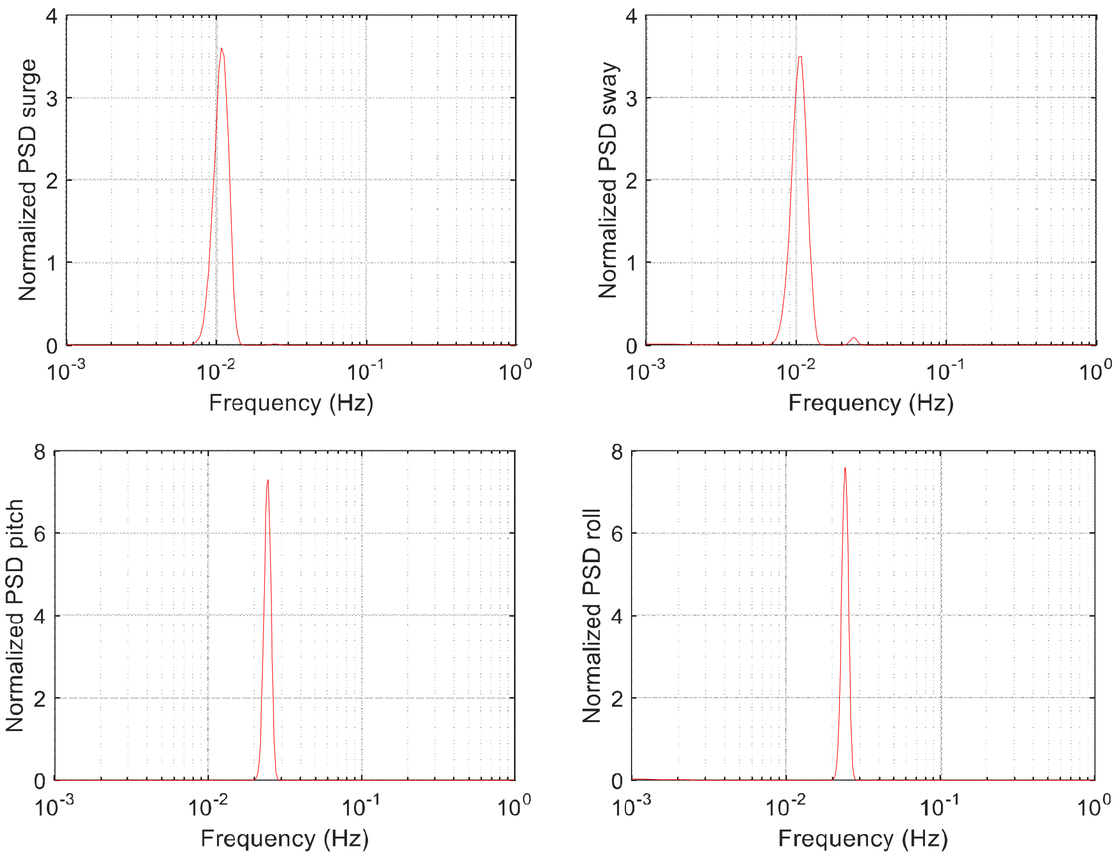

Figure 7. Normalized PSDFs from the free decay tests: surge and sway (top), pitch and roll (bottom).

The power in a band of 0.01 Hz around the natural frequency was evaluated and found to be in the order of 99% of the total power for the surge, roll and pitch motions, and in the order of 97.5% for the sway motion (Table 7). Notice that there is a slight difference between the surge and sway frequencies, deriving from the different angles of the moorings for the two directions on movement; in the following we shall refer to a common surge/sway frequency of 0.011, and a common roll/pitch frequency of 0.024.

Table 7. Natural periods and frequencies, band power and total power of surge, sway, roll and pitch motions.

D.o.F.	**Period [s]**	**Frequency [Hz]**	**Band power**		**Total power**	
Surge	88.5	0.0113	6.126	[m²]	6.171	[m²]
Sway	94.5	0.0106	23.97	[m²]	24.58	[m²]
Roll	41.5	0.0241	0.0220	[deg²]	0.0221	[deg²]
Pitch	40.9	0.0244	0.0096	[deg²]	0.0097	[deg²]

The damping ratio was calculated using the logarithmic decrement method, as a function of two response amplitudes X_j and X_{j+1} according to the following expression:

$$\xi = \frac{\delta}{\sqrt{4\pi^2 + \delta^2}} \tag{6}$$

where $\delta = (1/j)\ln(X_j/X_{j+1})$, j being the number of cycles taken into account.

To quantify the non-linear nature of damping, damping ratios were calculated considering different numbers of cycles, as shown in Figure 8. As expected, the damping ratios decrease with decreasing amplitude of oscillations. In particular, it is found that, besides the first cycle featuring a very large damping, the damping ratios stabilize at the second cycle, and become almost constant from the third cycle. In addition, damping appears to be only little dependent on D.o.F.; in particular values of 0.12, 0.19, 0.13 and 0.15 % were found for surge, sway, roll and pitch, respectively when the fourth cycle of oscillation was considered.

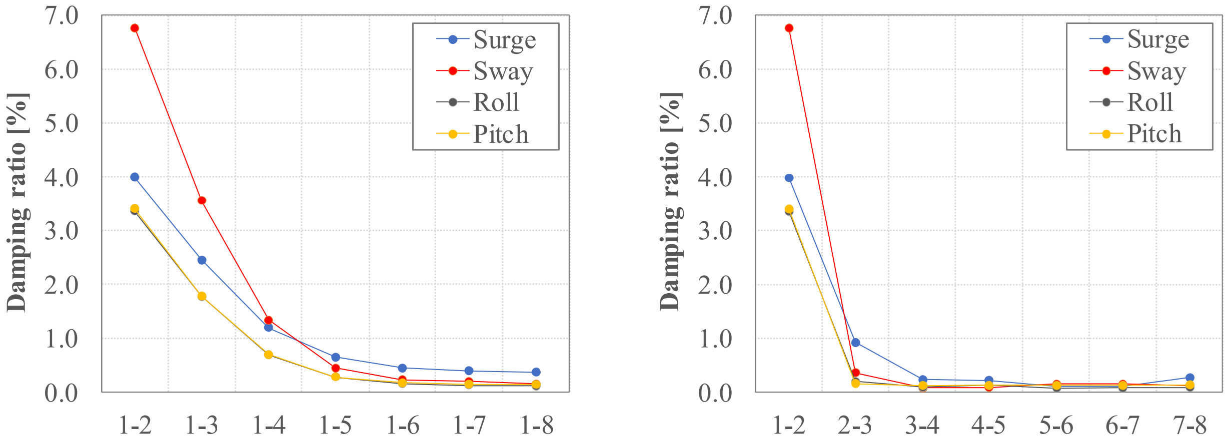

(a) (b)

Figure 8. Damping ratios for the surge, sway, roll and pitch motions from the free decay tests, obtained from the average logarithmic decrement considering: (*a*) the peaks X_1 and X_{j+1} and (*b*) consecutive pairs of peaks.

5.2 Dynamic response to regular waves

In this section, the measured displacements, rotations, accelerations and forces at the top and base of the tower are discussed in the time and frequency domains, for the selected tests given in Table 6.

As an example, in figure 9 the PSDF of sway as measured in test #1382 is shown. The natural sway frequency of 0.011 Hz and the wave frequency of 0.088 Hz are clearly identified. In addition, the first two harmonics of the wave frequency are also visible at 0.176 Hz and 0.264 Hz; these are the effect of second-order hydrodynamic excitation, in agreement with Browing *et al*. [33]. Finally, a spike is also clearly visible at a frequency of 1.6 Hz. These five frequencies are recognized in almost all measured signals, with different relative amplitudes, depending on wave height, rotor condition, and measured quantity. The peak at 1.6 Hz is postulated to correspond to the first elastic bending frequency of the system. This was calculated to be 0.4 Hz for the prototype structure [33], and if Cauchy scaling were matched, it should have been the same on the model. Indeed, Cauchy scaling was not considered in the design of the model, therefore elastic frequencies are not accurately reproduced by the model. This suggests that the measured signals be filtered in order to remove the frequencies at which elastic response occurs. In doing this one must be aware that if the elastic modes were properly reproduced in the model, these would have given a higher contribution to the total response than the one that is removed.

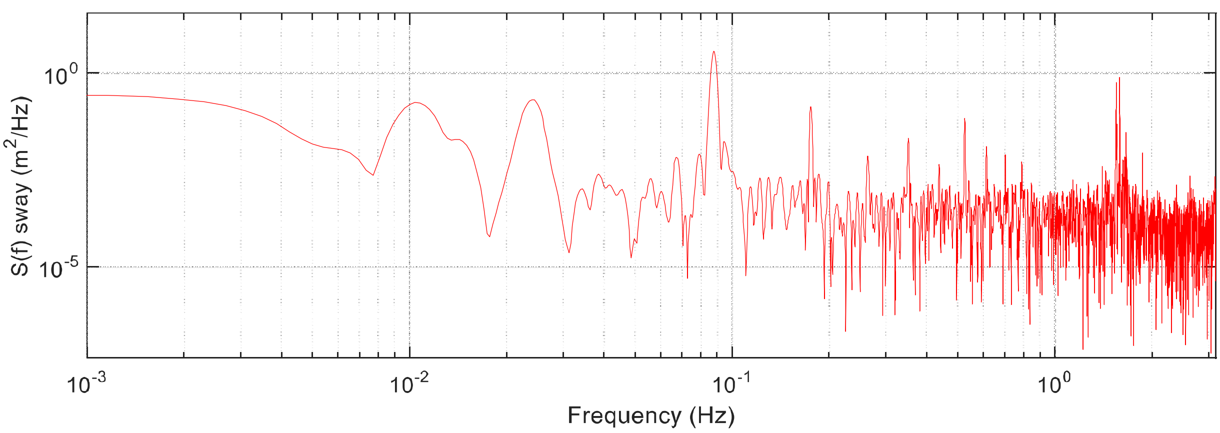

Figure 9. PSD of sway as measured in test #1382.

Again for test #1382, in Figure 10 sample time histories of surge, sway, roll, pitch, $a_{x,base}$ and $a_{y,top}$ are shown. It is noted that all the quantities associated with a longitudinal motion are almost sinusoidal, with a frequency of 0.088 Hz, indicating that the motion takes place at the excitation frequency. The remaining quantities, which are associated with a lateral motion, show a quite different behaviour. Both sway and roll feature two different components, one at a frequency of 0.088 Hz, associated with the external excitation acting in the longitudinal direction, and the other at 0.83 Hz for sway and at 1.6 Hz for roll, corresponding to the elastic frequency. For $a_{y,top}$ the response occurs mainly at 0.3 Hz.

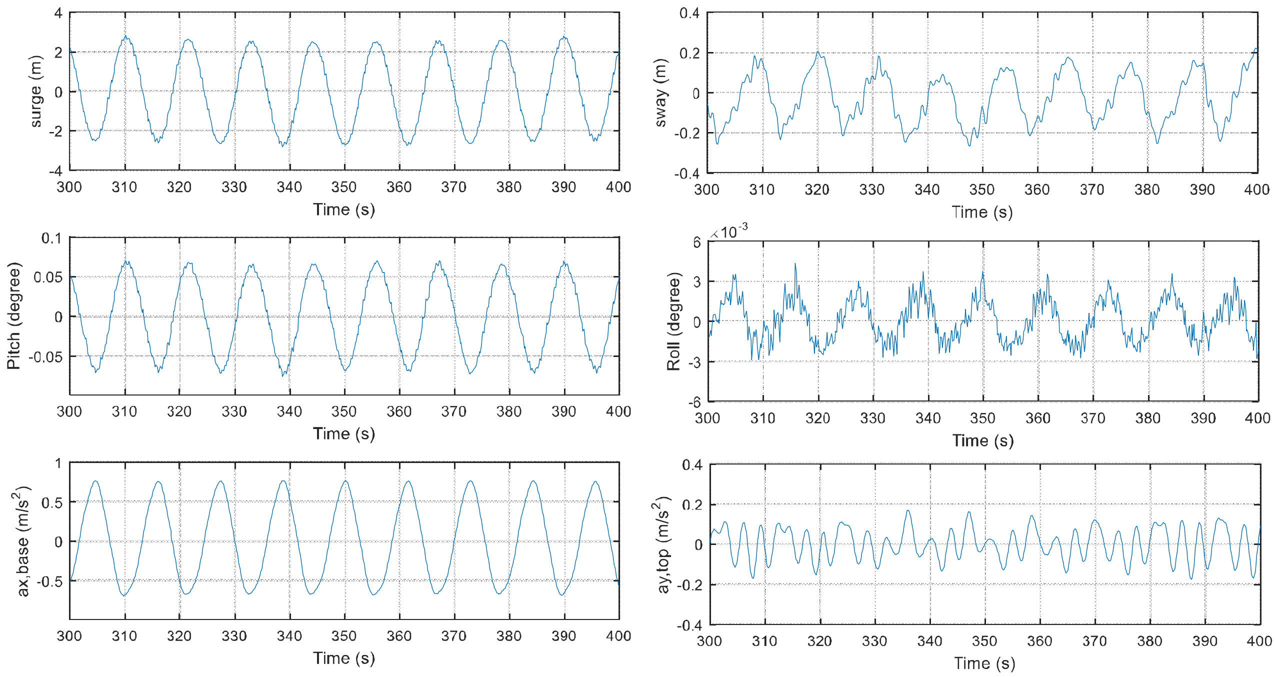

Figure 10. Sample time histories of surge, sway, roll, pitch, $a_{x,base}$ and $a_{y,top}$ as measured in test #1382.

The results discussed above where consistent among all the tests analysed, and this can be better seen from a frequency domain analysis.

In figure 11, the PSDFs of surge as measured in the eight tests listed in Table 6 are shown, together with a close-up view of the peaks at the first and second harmonic of the fundamental wave frequency. In all the tests the response is dominated by the wave frequency. It is noticed that in parked conditions the response increases with wave height at all frequencies of interest, whereas in operational conditions this trend is not always confirmed; this suggests that the gyroscopic effects and the rotor dynamics can somehow affect response.

Figure 12 shows, in the same format as Figure 11, the PSDFs of the longitudinal accelerations as measured in eight tests listed in Table 6, confirming the same results as those of Figure 12.

Figures 13 and 14 show the PSDFs of sway and of lateral accelerations as measured in eight tests listed in Table 6. For sway the wave frequency is not dominant, but most of the excitation is at the oscillation frequency; on the other hand, for the accelerations higher frequency components are amplified and the wave frequency is dominant again.

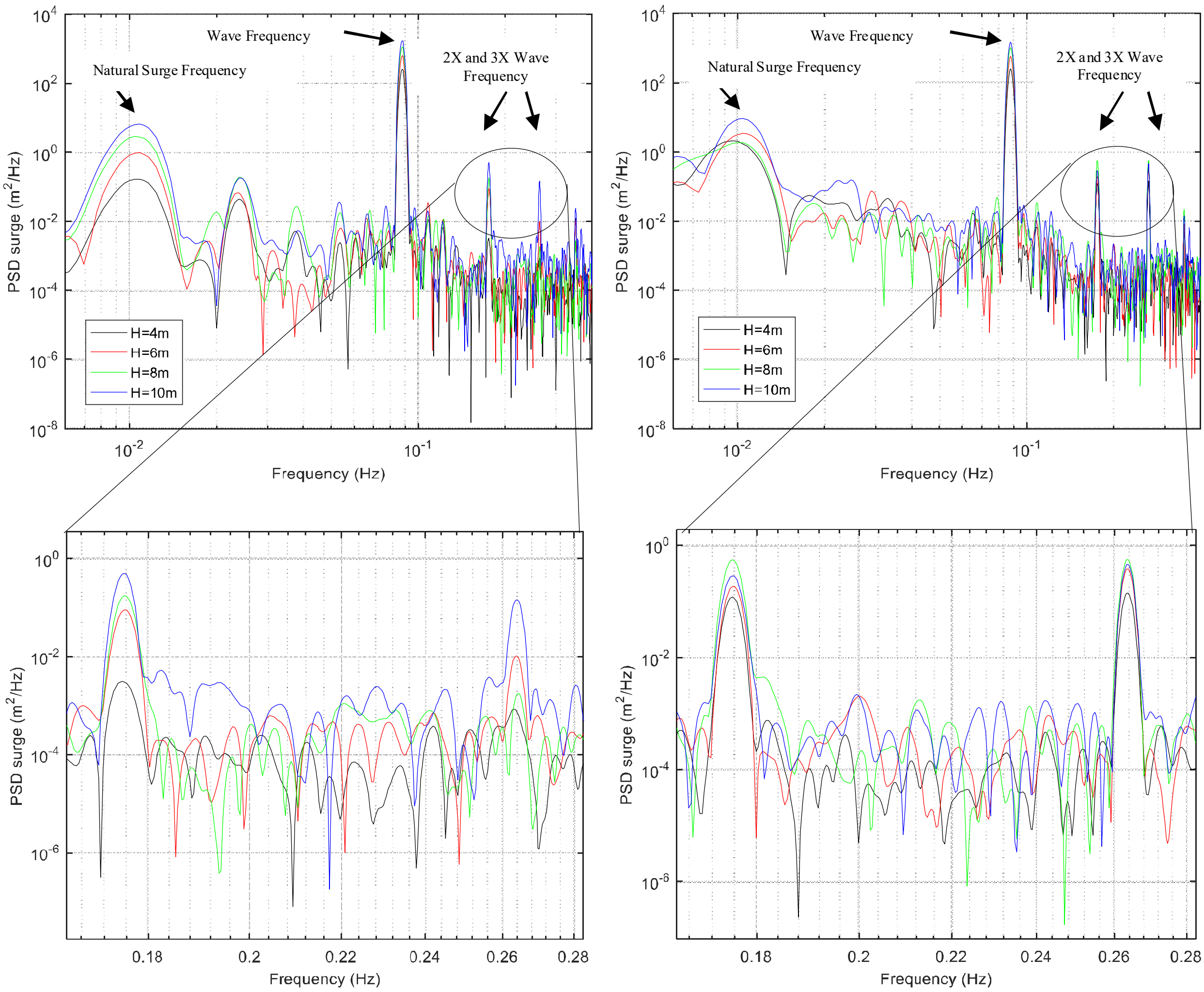

Figure 11. PSDFs of surge as measured in the different tests: parked conditions (left) and operational conditions (right). Close-up view of the peaks at the first and second harmonic of the wave frequency.

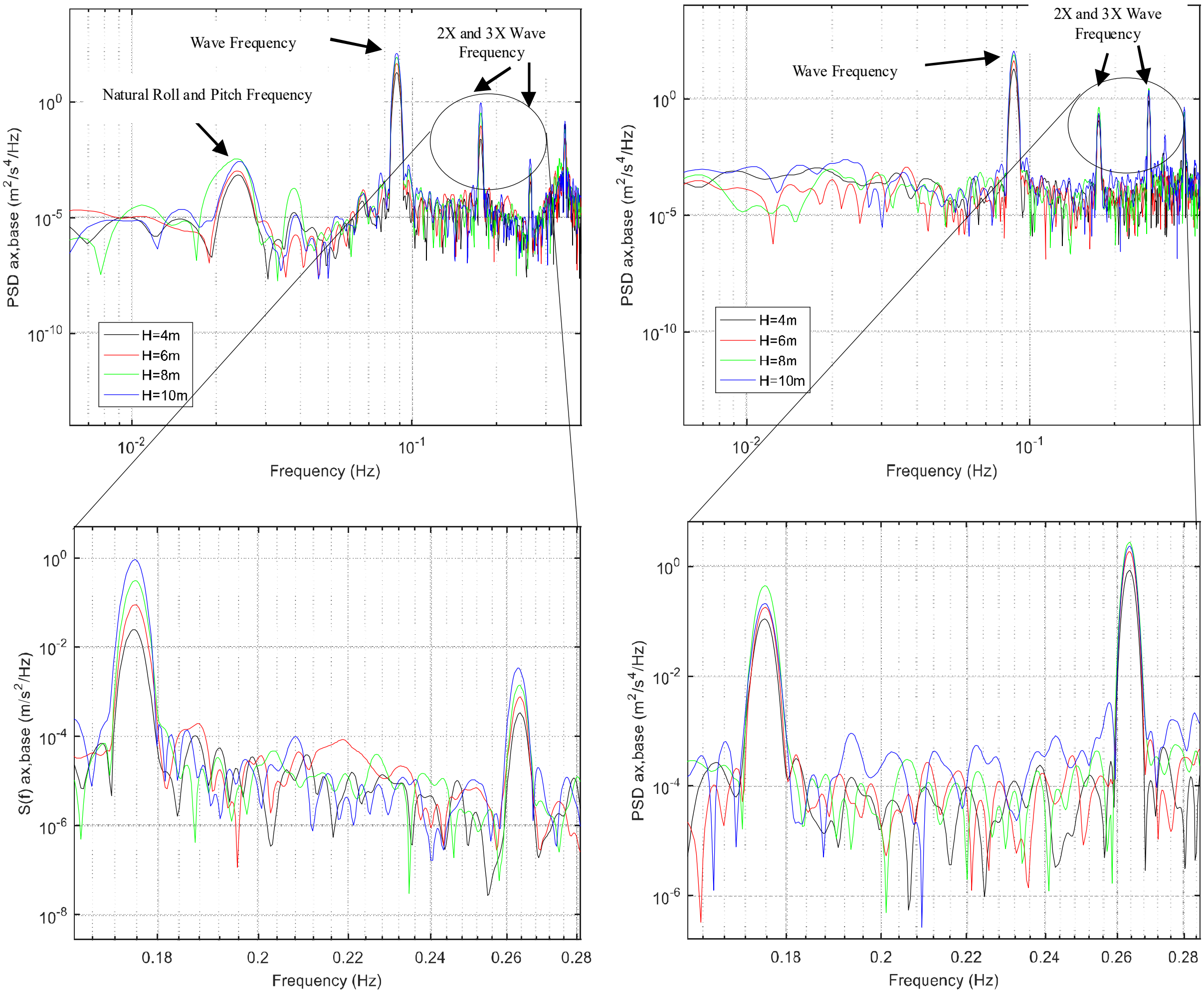

Figure 12. PSDFs of $a_{x,base}$ as measured in the different tests: parked conditions (left) and operational conditions (right). Close-up view of the peaks at the first and second harmonic of the wave frequency.

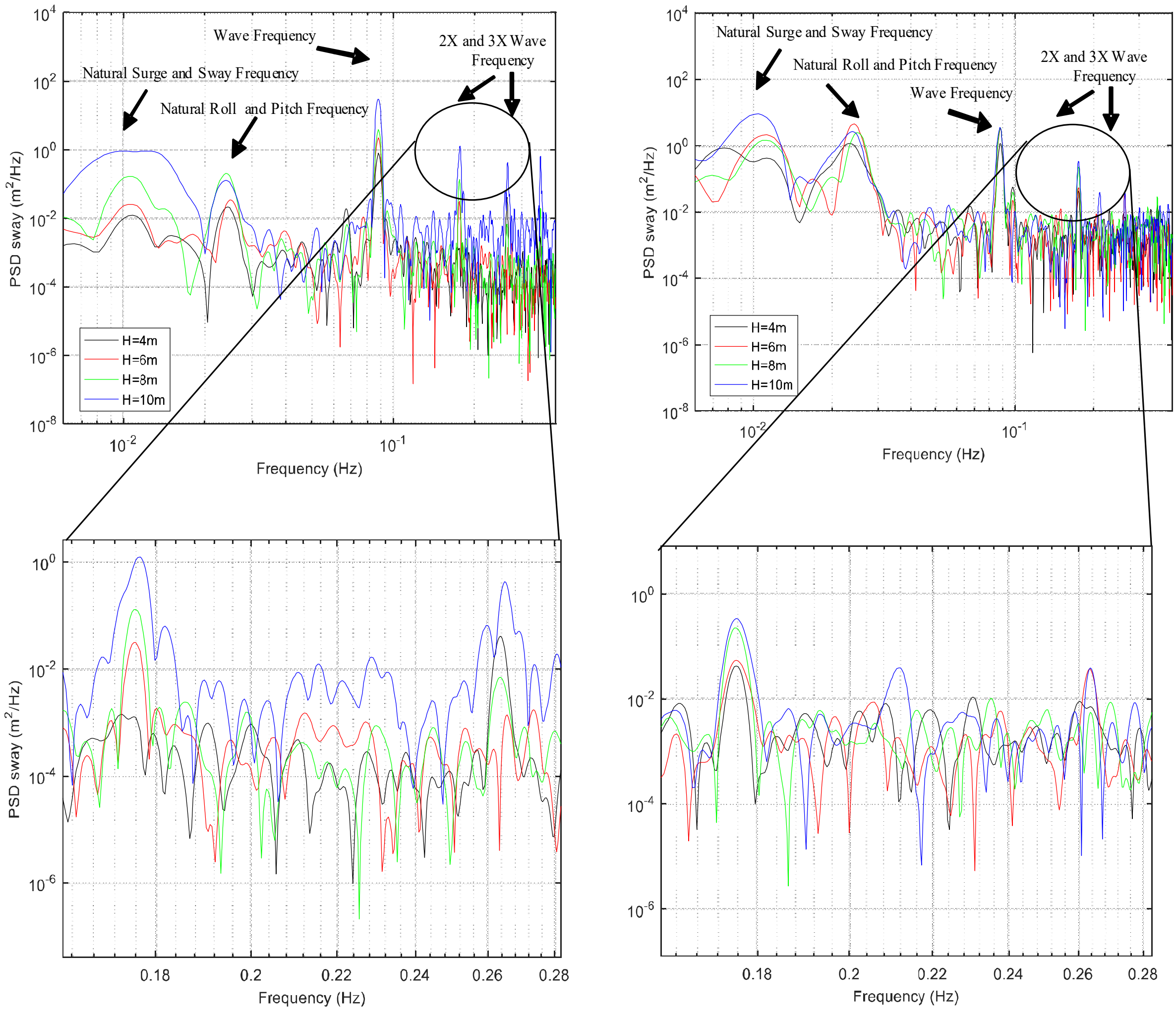

Figure 13. PSDFs of sway as measured in the different tests: parked conditions (left) and operational conditions (right). Close-up view of the peaks at the first and second harmonic of the wave frequency.

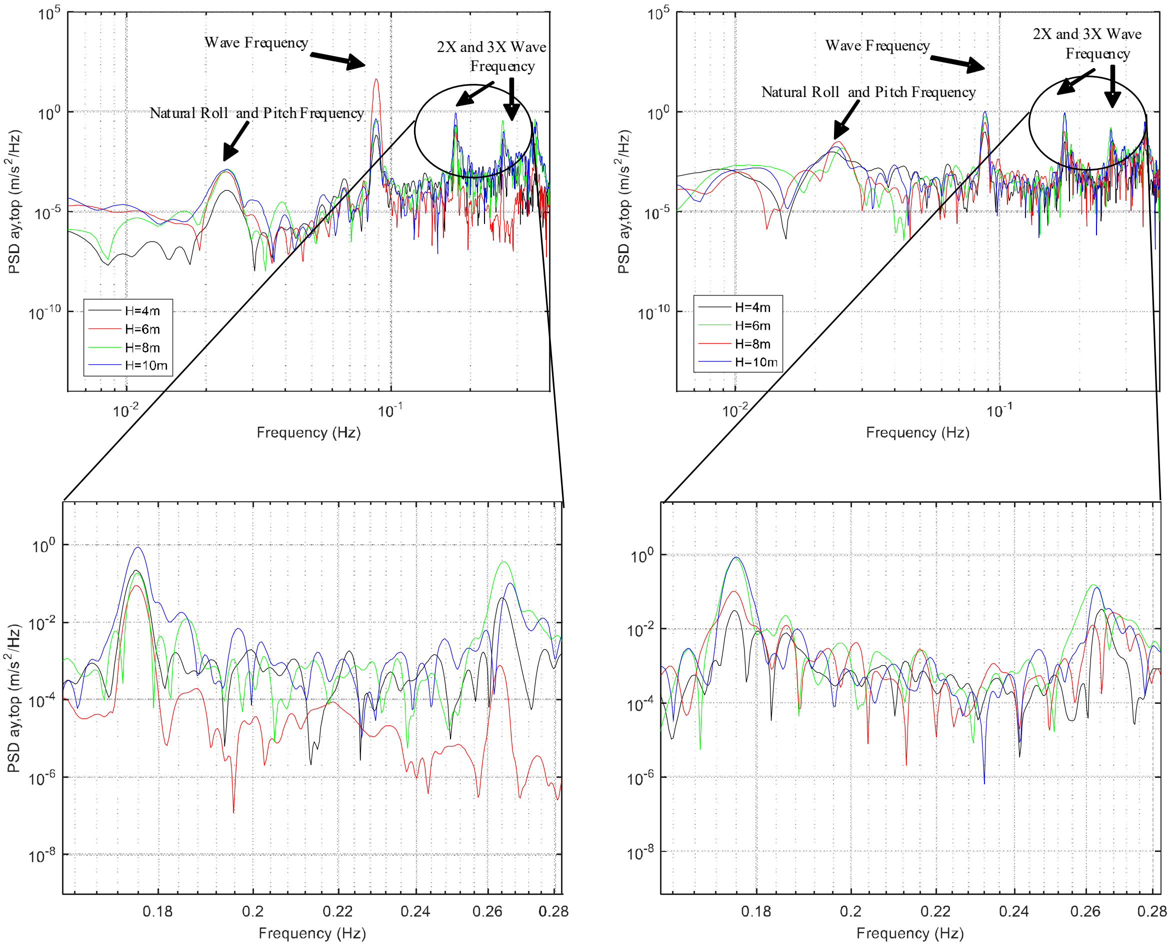

Figure 14. PSDFs of $a_{y,top}$ as measured in the different tests: parked conditions (left) and operational conditions (right). Close-up view of the peaks at the first and second harmonic of the wave frequency.

To quantify the contribution of the different frequencies to the total response, Tables 8 through 13 show the power corresponding to narrow ranges around the relevant frequencies, together with the total power. Tables 8, 10 and 12 show the quantities associated with the longitudinal response. It is observed that the fundamental wave frequency contributes to the total surge from 96.8% to 98.5%, to the total pitch from 97.1% to 99.1% and to the total longitudimal acceleration form 93.7% to 98.6%. Only in the case of the longitudinal acceleration there is a minor contribution of the second armonic of the wave frequency of up to 4.1%.

Table 8. Surge narrow-band and total power (m^2).

	Parked				Operational			
H (m)	4	6	8	10	4	6	8	10
Surge/Sway Frequency	5.42E-04	2.82E-03	8.58E-03	1.97E-02	6.98E-03	1.06E-02	7.46E-03	2.51E-02
Wave Frequency	7.79E-01	1.88E+00	3.37E+00	5.21E+00	7.77E-01	1.77E+00	3.17E+00	4.61E+00
2X Wave Frequency	1.26E-05	2.95E-04	5.62E-04	1.50E-03	3.62E-04	5.65E-04	1.69E-03	9.17E-04
3X Wave Frequency	3.86E-06	3.16E-05	4.95E-06	4.47E-04	4.42E-04	1.17E-03	1.70E-03	1.40E-03
Total power	7.92E-01	1.91E+00	3.42E+00	5.30E+00	8.03E-01	1.81E+00	3.23E+00	4.70E+00

Table 9. Sway narrow-band and total power (m^2).

	Parked				Operational			
H (m)	4	6	8	10	4	6	8	10
Sway/Surge Frequency	3.44E-05	7.36E-05	4.62E-04	4.73E-03	3.47E-03	6.53E-03	4.38E-03	3.05E-02
Wave Frequency	2.51E-03	6.94E-03	1.18E-02	9.91E-02	3.53E-03	9.44E-03	9.94E-03	1.17E-02
2X Wave Frequency	8.33E-06	9.06E-05	3.77E-04	4.38E-03	1.32E-04	2.21E-04	7.33E-04	1.24E-03
3X Wave Frequency	1.30E-04	4.72E-06	2.09E-05	1.56E-03	6.28E-05	1.28E-04	4.08E-08	1.19E-04
Total power	3.20E-03	7.90E-03	1.50E-02	1.25E-01	1.19E-02	4.34E-02	2.77E-02	6.21E-02

Table 10. Pitch narrow-band and total power (deg^2).

	Parked				Operational			
H (m)	4	6	8	10	4	6	8	10
Pitch/Roll Frequency	2.52E-07	5.18E-07	1.97E-06	9.84E-07	5.73E-07	3.29E-07	6.98E-07	1.76E-06
Wave Frequency	4.32E-04	1.14E-03	2.15E-03	3.03E-03	4.05E-04	9.20E-04	1.68E-03	2.32E-03
2X Wave Frequency	1.28E-06	7.27E-07	2.83E-06	3.94E-05	2.98E-07	3.61E-07	4.26E-07	5.16E-08
3X Wave Frequency	3.39E-08	2.56E-07	5.83E-08	8.40E-06	1.12E-06	1.33E-06	3.16E-06	1.97E-06
Total power	4.38E-04	1.15E-03	2.17E-03	3.13E-03	4.17E-04	9.33E-04	1.70E-03	2.35E-03

Table 11. Roll narrow-band and total power (deg^2).

	Parked				Operational			
H (m)	4	6	8	10	4	6	8	10
Roll/Pitch Frequency	2.67E-09	4.66E-09	1.48E-08	8.37E-08	2.84E-07	3.38E-07	4.49E-07	4.20E-07
Wave Frequency	2.95E-07	9.01E-07	1.77E-06	3.78E-06	3.79E-06	1.10E-05	2.28E-05	3.27E-05
2X Wave Frequency	1.07E-07	2.96E-09	4.19E-08	3.22E-06	1.01E-07	6.59E-08	1.46E-07	7.78E-08
3X Wave Frequency	2.07E-08	2.05E-09	7.16E-09	1.20E-06	3.00E-08	1.21E-08	2.38E-08	1.99E-08
Total power	4.25E-07	9.11E-07	1.83E-06	8.28E-06	4.21E-06	1.14E-05	2.34E-05	3.32E-05

Table 12. Acceleration $a_{x,base}$ narrow-band and total power (m^2/s^4).

	Parked				Operational			
H (m)	4	6	8	10	4	6	8	10
Pitch/Roll Frequency	2.07E-06	3.29E-06	1.43E-05	8.63E-06	8.56E-07	8.56E-07	2.85E-06	1.10E-05
Wave Frequency	5.61E-02	1.37E-01	2.48E-01	3.82E-01	5.63E-02	1.27E-01	2.30E-01	3.29E-01
2X Wave Frequency	7.63E-05	2.86E-04	9.54E-04	2.76E-03	3.39E-04	5.37E-04	1.34E-03	6.70E-04
3X Wave Frequency	1.08E-06	2.39E-06	4.40E-06	1.07E-05	2.56E-03	5.56E-03	8.32E-03	6.94E-03
Total power	5.71E-02	1.39E-01	2.52E-01	3.89E-01	6.01E-02	1.35E-01	2.43E-01	3.42E-01

Table 13. Acceleration $a_{y,top}$ narrow-band and total power (m^2/s^4).

	Parked				Operational			
H (m)	4	6	8	10	4	6	8	10
Roll/Pitch Frequency	4.20E-07	1.08E-06	4.12E-06	4.88E-06	5.90E-05	1.02E-04	4.93E-05	7.49E-05
Wave Frequency	2.12E-04	5.23E-04	1.10E-03	1.39E-03	3.21E-04	8.91E-04	1.92E-03	3.17E-03
2X Wave Frequency	7.15E-04	5.96E-04	5.18E-04	2.79E-03	9.26E-05	4.02E-04	2.62E-03	2.97E-03
3X Wave Frequency	1.61E-04	6.83E-04	1.76E-04	2.80E-03	1.28E-04	1.41E-04	8.29E-04	5.22E-04
Total power	1.21E-03	2.79E-03	5.62E-03	7.35E-03	1.44E-03	2.87E-03	7.57E-03	1.02E-02

Tables 9, 11 and 13, on the other hand, show the quantities associated with the lateral response. Only for sway in operational conditions, the fundamental wave frequency is not dominat, and contributes to the total response from 18.8% to 35.9%, whereas the oscillation frequency contributes to the total response from 15.1% to 49.1%; in this case there is also a contribution up to 32.9% at the roll frequency (not shown in the tables). For sway in parked conditions and for roll the wave frequency is dominant, with contributions to the total response from 78.4% to 87.8% for sway, and from 45.6% to 98.9% for roll; the lowest contributions of the wave frequency to roll are accompained by contributions at its first harmonic, so that the sum of the two components is always greater than 84.5%. For the lateral acceleration the wave frequency and its harmonics (up to the third) contribute to the total response from 50.7% to 89.9%. The variability of the total variance of the longitudinal response parameters with oncoming wave height is parabolic, and common to all parameters, regardless of the rotor condition (parked or operational); for the lateral response parameters the variability with wave height is not as regular, and dependent on the particular parameter and on the turbine condition.

To validate the values of damping calculated from the free decay tests, damping ratios at the dominant vibration frequency were calculated from the PSDFs through the half-power bandwidth method. For the case of the surge response, the damping ratio evaluated in the different tests is compared with that calculated from free decay in figure 15; the results obtained in parked conditions are in quite good agreement with each other and with those coming from free decay. On the other hand, it is observed that for operational conditions there is a minor scatter of the measured damping ratio calculated in stationary conditions, and some difference with that calculated from free decay with stationary rotor; these differences are ascribed to gyroscopic effects.

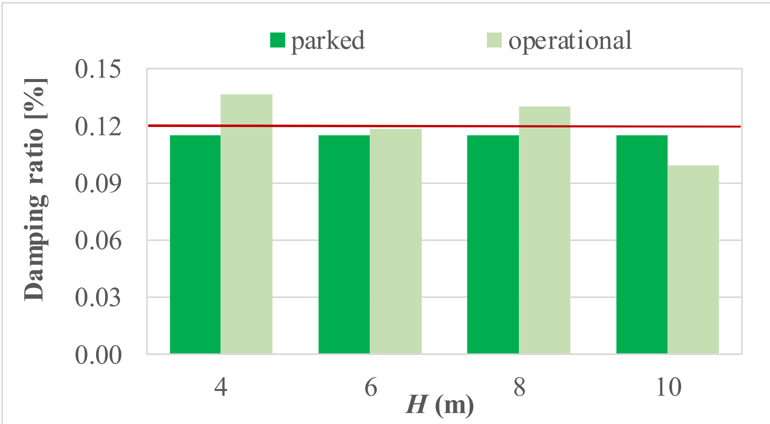

Figure 15. Damping ratios evaluated with the half-power bandwidth method in the surge D.o.F. for the different tests.

Finally, in figure 16, the histogram of the occurrence frequencies of surge, sway, roll, pitch, $a_{x,base}$ and $a_{y,top}$ as evaluated from test #1382 are shown. Consistently with what previously observed, it is noticed that the quantities related to the longitudinal response feature a bimodal distribution, indicating an almost sinusoidal response. On the other hand, the histograms of the quantities related to the lateral response are rather different from the previous ones, and from one another; these appear to be associated with the combination of a narrowband process and a broader band process, whose relative intensity depends on the particular quantity observed.

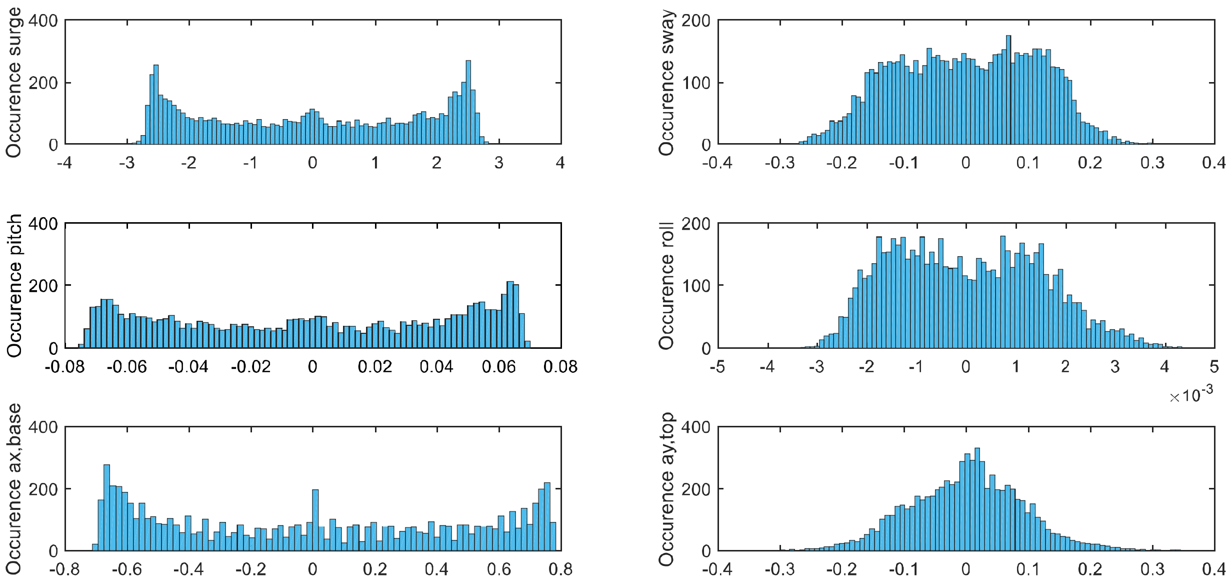

Figure 16. Histograms of the occurrence frequencies of surge, sway, roll, pitch, $a_{x,base}$ and $a_{y,top}$ as measured in test #1382.

5.3 Dynamic forces

Somehow similar conclusions to those presented for displacements and accelerations can be drawn for internal forces. In the same format as that of Tables 8 to13, Tables 14 through 17 show the power corresponding to narrow ranges around the relevant frequencies, together with the total power of four of the force components measured in the experiments. The wave frequency is always dominant, with contributions ranging from 84.6% to 97.7% for the longitudinal forces, and from 50.4% to 84.8% for the lateral forces. To the lowest components at the wave frequency, components at the first and second harmonics are associated, so that the sum is never lower than 74.4%.

Table 14. Force $F_{x,base}$ narrow-band and total power (MN^2).

	parked				Operational			
H (m)	4	6	8	10	4	6	8	10
Pitch/Roll Frequency	1.26E-05	3.30E-05	1.24E-04	1.02E-04	2.30E-05	7.97E-06	8.55E-06	1.07E-04
Wave Frequency	8.47E-01	2.10E+00	3.83E+00	6.82E+00	8.78E-01	1.99E+00	3.54E+00	7.21E+00
2X Wave Frequency	3.47E-03	1.27E-02	4.07E-02	9.44E-02	7.18E-04	1.58E-02	9.04E-02	2.08E-03
3X Wave Frequency	1.66E-03	5.19E-03	2.16E-02	3.05E-02	5.48E-02	9.42E-02	2.78E-01	1.52E-01
Total power	8.68E-01	2.15E+00	3.94E+00	7.03E+00	9.53E-01	2.13E+00	3.96E+00	7.53E+00

Table 15. Force $F_{y,base}$ narrow-band and total power (MN^2).

	parked				Operational			
H (m)	4	6	8	10	4	6	8	10
Roll/Pitch Frequency	2.29E-06	4.93E-06	2.62E-05	2.35E-05	3.79E-04	5.08E-04	2.75E-04	3.62E-04
Wave Frequency	1.57E-02	3.49E-02	5.75E-02	1.73E-01	1.35E-02	3.38E-02	5.67E-02	8.61E-02
2X Wave Frequency	2.41E-03	1.97E-03	8.66E-04	2.04E-02	6.76E-04	4.11E-03	2.31E-02	1.68E-02
3X Wave Frequency	6.65E-04	2.90E-03	3.90E-03	1.16E-03	1.62E-03	2.03E-03	3.30E-03	8.28E-04
Total power	1.87E-02	4.29E-02	7.09E-02	2.04E-01	1.90E-02	4.61E-02	9.13E-02	1.15E-01

Table 16. Force $F_{x,top}$ narrow-band and total power (MN^2).

	parked				Operational			
H (m)	4	6	8	10	4	6	8	10
Pitch/Roll Frequency	7.77E-06	1.15E-05	5.26E-05	3.05E-05	1.99E-05	7.93E-06	1.50E-05	6.14E-05
Wave Frequency	4.23E-01	0.10E+01	0.18E+01	0.29E+01	4.93E-01	0.11E+01	0.21E+01	0.30E+01
2X Wave Frequency	1.55E-03	6.47E-03	2.16E-02	6.38E-02	3.93E-04	5.67E-03	2.33E-02	1.86E-02
3X Wave Frequency	1.27E-03	4.11E-03	1.45E-02	2.89E-02	7.54E-02	1.66E-01	3.83E-01	1.38E-01
Total power	4.34E-01	0.11E+01	0.19E+01	0.30E+01	5.68E-01	0.13E+01	0.24E+1	0.32E+01

Table 17. Force $F_{y,top}$ narrow-band and total power (MN^2).

	parked				Operational			
H (m)	4	6	8	10	4	6	8	10
Roll/Pitch Frequency	1.31E-06	2.12E-06	9.72E-06	9.57E-06	1.54E-04	2.07E-04	1.12E-04	1.52E-04
Wave Frequency	4.16E-03	9.17E-03	1.51E-02	1.67E-02	5.57E-03	1.68E-02	3.06E-02	4.30E-02
2X Wave Frequency	1.59E-03	1.26E-03	7.97E-04	7.14E-03	4.45E-04	1.53E-03	1.04E-02	9.04E-03
3X Wave Frequency	4.48E-04	1.82E-03	3.45E-03	1.43E-03	4.07E-04	5.82E-04	1.55E-06	8.22E-04
Total power	6.63E-03	1.48E-02	2.60E-02	3.31E-02	9.52E-03	2.39E-02	4.92E-02	6.20E-02

Comparison between the measured displacements and corresponding forces is shown in figure 18. It is observed that RMS surge is a meaningful measure of the dynamic response, being the measured forces in general monotonically increasing with it. This happens in particular for the longitudinal forces, which are clearly associated with the longitudinal inertia; for the lateral forces no relation to the longitudinal inertia is expected, however, the trend is still reasonably good.

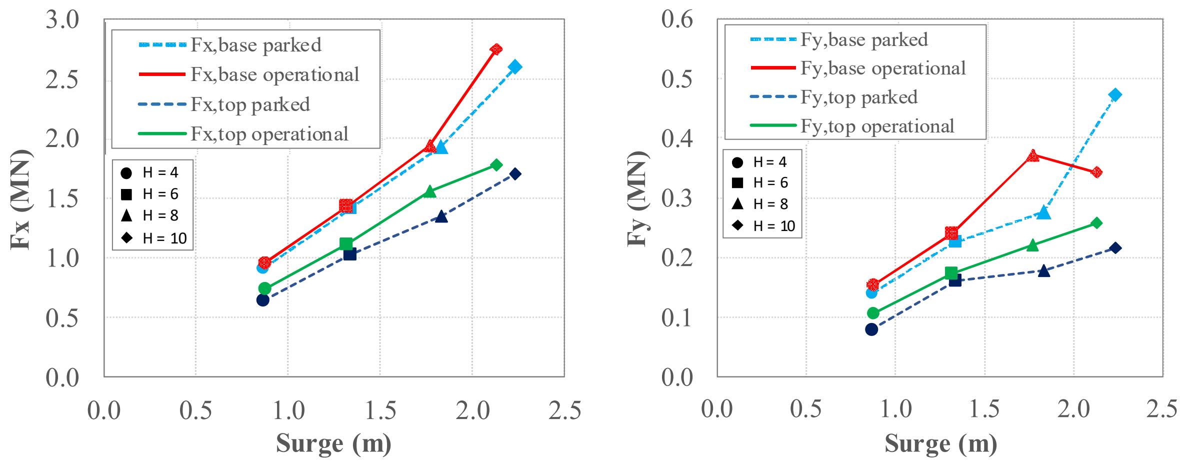

(a) (b)

Figure 18. STD of the measured force as a function of the STD of surge in (*a*) longitudinal and (*b*) transverse directions.

5.4 Peak factors and expected maxima

The experimental results presented can be used to evaluate the expected maxima of the response parameters. In Table 18 the STD of the ten discussed response parameters (displacements, rotations, accelerations and forces) are summarised for the eight tests.

Table 18. STD of displacements, rotations, accelerations and forces.

	parked				operational			
H (m)	4	6	8	10	4	6	8	10
Surge (m)	0.8672	1.340	1.833	2.234	0.8758	1.317	1.770	2.130
Sway (m)	0.0566	0.0889	0.1072	0.3536	0.1091	0.2083	0.1664	0.2492
Pitch (deg)	0.0204	0.0330	0.0458	0.0576	0.0199	0.0362	0.0407	0.0759
Roll (deg)	0.0007	0.0010	0.0014	0.0040	0.0023	0.0036	0.0050	0.0059
$a_{x,base}$ (m/s^2)	0.2330	0.3617	0.4893	0.6099	0.2396	0.3608	0.4821	0.5740
$a_{y,top}$ (m/s^2)	0.0348	0.0529	0.0750	0.0857	0.0380	0.0536	0.0870	0.1012
$F_{x,\mathrm{base}}$ (MN)	0.9086	1.420	1.933	2.598	0.9566	1.427	1.938	2.748
$F_{y,\mathrm{base}}$ (MN)	0.1402	0.2071	0.2663	0.4521	0.1378	0.2148	0.3022	0.3392
$F_{x,\mathrm{top}}$ (MN)	0.6426	1.024	1.352	1.702	0.7396	1.112	1.560	1.776
$F_{y,\mathrm{top}}$ (MN)	0.0815	0.1218	0.1611	0.1818	0.0959	0.1547	0.2219	0.2483

To the aim of obtaining expected response peak values, the peak factors were determined according to Vanmarcke [34, 35].

The spectral moments were computed by numerical integration. The peak factors for surge, pitch and longitudinal acceleration and forces have been calculated based on the bimodal PSD method; the concept of bimodal PSD can be generalized including all the structural responses with two dominant frequency ranges [36]. The overall dynamic process has been analysed applying two different approaches for the different spectral bands, to define a combined peak factor. In particular, the first approach considers the spectral band around the wave frequency as a very narrow band process. Thus, the corresponding peak factor g_{x1} of a sinusoidal process, equal to $\sqrt{2}$ was assumed. The second approach was applied to the remaining, higher frequency range, as a Gaussian process. Accordingly, the Vanmarcke approach was applied to calculate the corresponding peak factor g_{x2}. Finally, to evaluate the overal maximun response, the Square Root of the Sum of the Squares (SRSS) rule was used to combine the two peak response components [37] as follow:

$$Max\,value = \sqrt{g_{x1}^2\,\sigma_{x1}^2 + g_{x2}^2\,\sigma_{x2}^2} \tag{7}$$

where σ_{x1}^2 and σ_{x2}^2 are the variance of the two parts of the dynamical process, calculated from the corresponding spectral moment.

The peak factors for sway, roll and lateral acceleration and forces have been calculated based only on the approach proposed by Vanmarcke, applying to Gaussian, narrowband processes.

The peak factors calculated as above, over a duration of 1,053 seconds, that represent the duration of the tests, are summarized in Table 18, together with the measured peak factors (in brackets, max/STD) over the same record.

It is observed that the prediction of the peak factor of the longitudinal components of the response is quite accurate, with average errors in the order of 9% in parked conditions and 11% in operational conditions. This indicates that the bimodal method performs well in this case. On the other hand, the prediction of the peak factor of the lateral components of the response is much more scattered and less accurate, with errors ranging from 2% to 100%. This is due to the fact that some of the lateral components of the response are nearly Gaussian (e.g. $a_{y,top}$), in which case the prediction is fairly accurate; in some others they are quite away from being Gaussian (e.g. $F_{y,base}$), and the prediction is very inaccurate.

Table 18. Calculated (measured) peak factors of displacements, rotations, accelerations and forces.

	Parked				Operational			
H (m)	4	6	8	10	4	6	8	10
Surge	1.44 (1.49)	1.43 (1.52)	1.43 (1.53)	1.43 (1.55)	1.46 (1.83)	1.44 (1.64)	1.43 (1.66)	1.43 (1.74)
Sway	3.54 (2.43)	3.47 (2.25)	3.51 (2.65)	3.57 (2.92)	3.60 (3.56)	3.40 (3.83)	3.52 (4.13)	3.42 (3.21)
Pitch	1.47 (1.43)	1.44 (1.49)	1.44 (1.47)	1.52 (1.70)	1.54 (1.82)	1.47 (1.80)	1.46 (1.71)	1.46 (1.71)
Roll	3.60 (2.60)	3.55 (2.11)	3.57 (2.64)	3.73 (3.00)	3.56 (3.23)	3.45 (2.15)	3.43 (1.99)	3.41 (1.88)
$a_{x,base}$	1.45 (1.58)	1.43 (1.56)	1.43 (1.60)	1.45 (1.72)	1.64 (1.68)	1.60 (1.71)	1.58 (1.80)	1.52 (1.77)
$a_{y,top}$	3.45 (2.73)	3.57 (3.40)	3.58 (3.80)	3.57 (4.86)	3.75 (3.25)	3.70 (3.64)	3.63 (3.23)	3.62 (3.55)
$F_{x,\mathrm{base}}$	1.47 (1.65)	1.45 (1.68)	1.47 (1.69)	1.49 (1.67)	1.67 (1.47)	1.62 (1.53)	1.74 (1.59)	1.55 (1.49)
$F_{y,\mathrm{base}}$	3.37 (1.66)	3.43 (2.29)	3.47 (2.67)	3.38 (2.56)	3.45 (2.78)	3.45 (1.92)	3.44 (2.39)	3.45 (2.56)
$F_{x,\mathrm{top}}$	1.50 (1.71)	1.45 (1.75)	1.49 (1.74)	1.53 (1.71)	1.90 (1.84)	1.84 (1.66)	1.91 (1.61)	1.66 (1.70)
$F_{y,\mathrm{top}}$	3.43 (2.09)	3.52 (2.96)	3.56 (3.13)	3.54 (2.74)	3.57 (3.18)	3.53 (2.49)	3.49 (2.93)	3.49 (2.74)

5.5 Mooring lines forces

Analysis of the mooring line forces revealed a strong sensitivity of the measured data on the alignment of the lines with the oncoming waves. In the experimental setup mooring line 1 was aligned with the oncoming waves and the mooring lines 2 and 3 were symmetric at an angle of 120° with mooring line 1 (Figure 19a). The analysis of measured forces indicated an asymmetric behaviour, which was ascribed to a no perfect alignment in the setup. In Figure 19a a sample time history of the force measured in test #1380 is shown, clearly indicated the non-symmetric behaviour. Therefore, a correction was applied to the force components, minimizing the difference between the measured mean force in lines 2 and 3. This procedure indicated a misalignment of the experimental setup of 3.63° with respect to the oncoming wave direction. In figure 19b the corrected sample time histories for test #1380 are shown; in the corrected time histories line 1 is aligned with the oncoming wave direction, but a slight asymmetry between lines 2 and 3 is still present, indicating a discrepancy between the actual angles between line 1 and lines 2 and 3, and the theoretical value of 120°. These latter experimental error cannot be corrected with post processing.

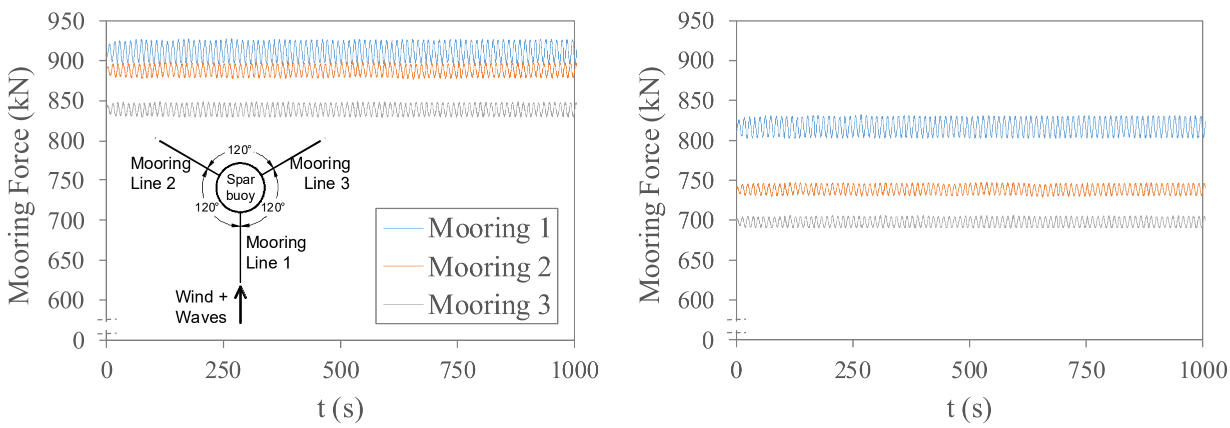

(a) (b)

Figure 19. Sample time histories of mooring line forces for test #1380: raw data (a), corrected data (b).

In Figure 20 the PSDFs of the mooring line 1 tension for the parked and operational conditions are shown. Like displacement and acceleration spectra, shown in figures 11 to 14, the surge, sway, pitch and roll oscillations frequencies are clearly visible, together with the oncoming wave frequency and first and second harmonics; in addition, the heave natural oscillation frequency is also visible at 0.034 Hz. Heave response appears to be more than linearly increasing with wave height. Table 21 shows the power corresponding to narrow ranges around the relevant frequencies, together with the total power of the force in mooring line 1. In this case, almost all the energy is concentrated at the wave frequency, from 97.3% to 99.2% of the total power. Globally it is observed that the dynamic forces in the mooring lines are larger in parked conditions than in operational conditions, essentially due to the different dynamic response of the system coming from the presence of aerodynamic damping.

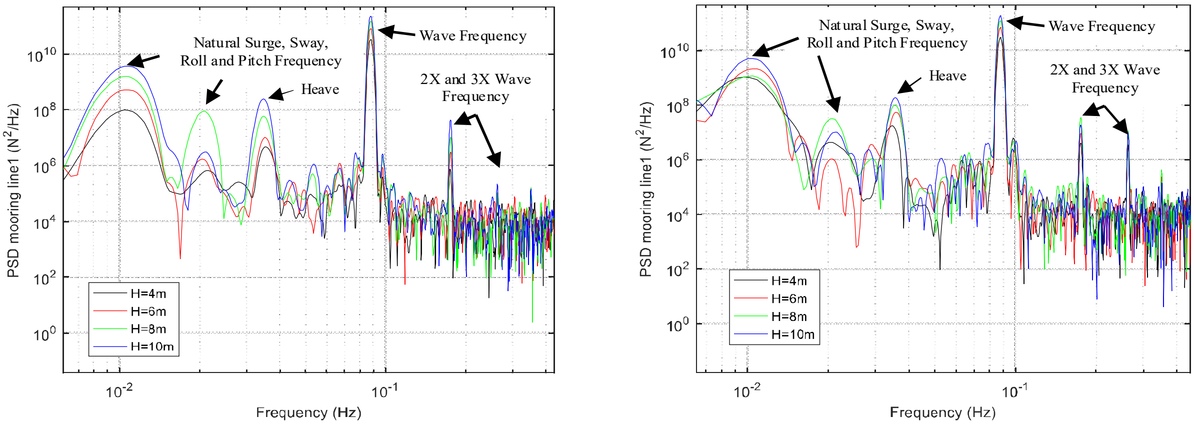

Figure 20. PSDFs of forces in mooring line 1 for parked (left) and operational (right) conditions.

Table 21. Mooring line 1 force narrowband and total power (N^2).

	Parked				Operational			
H (m)	4	6	8	10	4	6	8	10
Surge/Sway Frequency	2.13E+05	1.47E+06	4.01E+06	9.61E+06	1.83E+06	4.66E+06	3.24E+06	1.08E+07
Pitch/Roll Frequency	9.13E+02	3.63E+03	1.56E+05	1.12E+04	1.74E+04	8.94E+03	5.77E+04	4.37E+04
Heave Frequency	7.72E+03	2.08E+04	8.61E+04	5.33E+05	2.96E+04	7.22E+04	1.84E+05	3.49E+05
Wave Frequency	1.02E+08	2.50E+08	4.49E+08	6.95E+08	9.34E+07	2.17E+08	3.90E+08	5.86E+08
2X Wave Frequency	2.95E+03	9.89E+03	3.31E+04	1.32E+05	1.52E+04	3.16E+04	1.16E+05	5.03E+04
3X Wave Frequency	2.92E+02	5.29E+02	3.31E+04	1.47E+03	1.07E+04	2.51E+04	3.32E+04	2.75E+04
Total power	1.03E+08	2.52E+08	4.54E+08	7.06E+08	9.60E+07	2.23E+08	3.95E+08	5.99E+08

In Figure 21 a sample time history and the histogram of the occurrence frequencies of the force in mooring line 1 as measured in test #1380, are shown. As expected, it appears that the process is almost sinusoidal, with a minor component at a higher frequency. This suggests that the bimodal method is used for evaluating the peak factors. In Table 22 the mean, STD and calculated and measured peak factors of the force in mooring line 1, are given. Also in this case the dynamic forces are proportional to the oncoming wave height, whereas the mean forces are very little affected by it. Comparison between the calculated and measured values of the peak factors indicate that calculated values are almost coincident with the value of $\sqrt{2}$ applying to a sinusoidal process, whereas the measured value is some 13% larger, indicating the presence of higher frequency component.

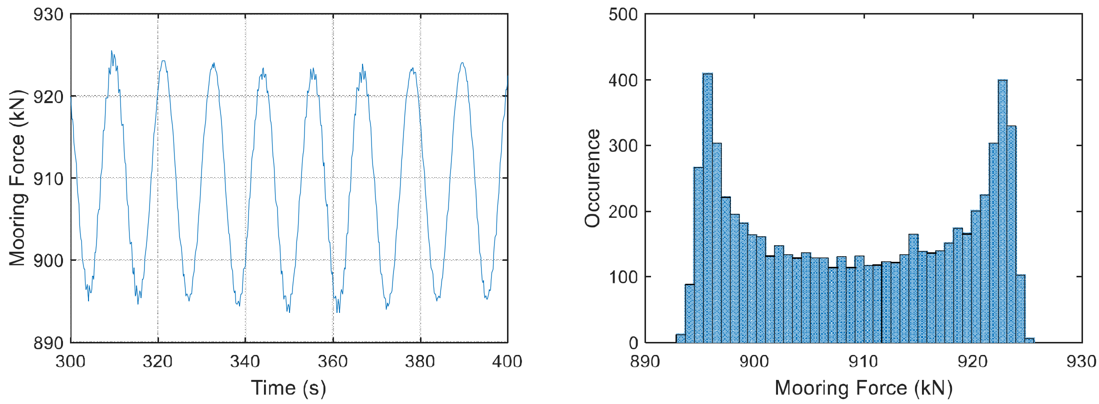

Figure 21. Sample time history and histogram of the occurrence frequencies of the force in mooring line 1 as measured in test #1380.

Table 22. Mean, STD and calculated (measured) peak factor of the force in mooring line 1.

	Parked				Operational			
H (m)	4	6	8	10	4	6	8	10
Mean [kN]	909.3	909.9	911.0	924.3	1249.6	1254.4	1263.0	1246.9
STD [kN]	10.13	15.85	21.30	26.56	9.76	14.88	19.81	24.42
Peak factor	1.42 (1.64)	1.42 (1.64)	1.42 (1.69)	1.42 (1.55)	1.43 (1.63)	1.42 (1.63)	1.42 (1.67)	1.42 (1.63)

6. CONCLUSIONS

In this paper, the feasibility of wave basin tests for investigating the dynamic response of a Spar Buoy Wind Turbine, has been investigated. Different regular and irregular wave heights have been considered, together with three different wind conditions. Displacements, accelerations, tower forces and mooring line forces have been measured and analysed.

First, free decay tests were carried out to detect the natural periods and the damping ratios. The measured full-scale rigid body oscillation frequencies were found to be 0.011 Hz in surge and sway and 0.024 Hz in pitch and roll. From measurement of the mooring line tensions in forced vibrations, also the heave frequency could be detected and found to be 0.034 Hz. The damping ratios coming from free decay test were compared with those measured in forced vibrations, showing a good agreement. In particular, values of 0.12%, 0.19%, 0.13% and 0.15% were found from free decay oscillations for surge, sway, roll and pitch, respectively when the fourth cycle of oscillation is considered. As a matter of comparison from forced vibration tests on the parked wind turbine a constant value of 0.12 was found for surge, and values in the range of 0.10 and 0.14 for operational conditions with a mean value of 0.12.

Analysis of the dynamic response in terms of displacements, accelerations and tower and mooring line forces reveals that this occurs mainly at the oncoming wave frequency, with smaller or larger components at its first and second harmonics. A component of the response was also found at the first elastic bending frequency of the tower; this, however, was not properly scaled, as the Cauchy number was not considered in the design of the model.

In particular, for the parameters associated with the longitudinal response in all tests the response is dominated by the wave frequency. It is noticed that in parked conditions the response increases with wave height at all frequencies of interest, whereas in operational conditions this trend is not always confirmed; this suggests that the gyroscopic effects and the rotor dynamics can somehow affect response. On the other hand, for the parameters associated with the lateral response the wave frequency is not always dominant and also the other harmonics are excited.

The comparison between the measured displacements and the corresponding tower forces highlights as the RMS of the surge is a meaningful measure of the dynamic response, being the measured forces in general monotonically increasing with it. This happens in particular for the longitudinal forces, which are clearly associated with the longitudinal inertia; however, for the lateral forces, the trend is still reasonably good.

Finally, peak factors were calculated using the bimodal methods for the longitudinal response components and using the Vanmarcke method for the lateral response components. The first proved to be rather accurate, whereas the second is more or less accurate depending on the parameter under investigation and on the rotor condition; this due to the more or less Gaussian nature of the process.

It can be concluded that wave basin tests are a useful tool for investigating the dynamic response of Spar Buoy Wind Turbine, provided that both Froude and Cauchy scaling are taken into account.

ACKNOWLEDGEMENTS

The present research has been supported by the EU Seventh Framework Programme (FP7) through the grant to the budget of the Integrated Infrastructure Initiative HYDRALAB IV (Contract Number: 261520) within the Transnational Access Activities.

REFERENCES

[1] W. E. Heronemus, Pollution-free energy from offshore winds, 8th Annual Conference and Exposition Marine Technology Society, Washington D.C., September 11-13, 1972.

[2] S. Butterfield, W. Musial, J. Jonkman, P. Sclavounos, Engineering challenges for floating off-shore wind turbines, Technical Report NREL/TP-500-38776 (2007).

[3] F. Aristodemo, G.R. Tomasicchio, P. Veltri, New model to determine forces at on-bottom slender pipelines. Coastal Engineering 58 (2011), pp. 267-280.

[4] B.M. Sumer, J. Fredsoe, Hydrodynamics around cylindrical structures, Advanced Series on Coastal Engineering, 12, World Scientific, Singapore (2006).

[5] J. Jonkman, D. Matha, A quantitative comparison of the responses of three floating platforms. Proceedings of European Offshore Wind 2009 Conference and Exhibition, NREL/CP-500-46726 (2009).

[6] G. Salvadori, F. Durante, G.R. Tomasicchio, F. D'Alessandro, Practical guidelines for the multivariate assessment of the structural risk in coastal and off-shore engineering, Coastal Engineering 95 (2015), pp. 77-83.

[7] G. Salvadori, G.R. Tomasicchio, F. D'Alessandro, Multivariate approach to design coastal and off-shore engineering, Journal of Coastal Research Special Issue (65) 1, (2013), pp. 386-391.

[8] G. Salvadori, G.R. Tomasicchio, F. D'Alessandro, Practical guidelines for multivariate analysis and design in coastal engineering, Coastal Engineering 88 (2014), pp. 1-14.

[9] C.H. Lee, WAMIT Theory Manual, MIT Report 95-2, Dept. of Ocean Eng., MIT (1995).

[10] C.H. Lee, Wave interaction with huge floating structure, BOSS'97, Delft, The Netherlands (1997).

[11] J. N. Newman, P. D. Sclavounos, The computation of wave loads on large offshore structures, Proceedings 5th International Conference on the Behaviour of Offshore Structures BOSS `88 Trondheim, Norway (1988).

[12] J. Jonkman, Definition of the floating system for phase IV of OC3, Technical Report NREL/TP-500-47535 (2010).

[13] M. Karimirad, T. Moan, Wave and wind induced motion response of catenary moored spar wind turbine, Int. Conf. on Computational Methods in Marine Engineering, International Center for Numerical Methods in Engineering (CINME), Barcelona, Spain (2009).

[14] T.J. Larsen, T.D. Hanson A method to avoid negative damped low frequent tower vibrations for a floating, pitch controlled wind turbine, J. Phys. Conf. Ser. 75 (2007) 012073.

[15] F.G. Nielsen, T.D. Hanson, B. Skaara, Integrated dynamic analysis of floating offshore wind turbine. Proc. Int. Conf. on Ocean, Offshore and Arctic Engineering, Am. Soc. Mech. Eng. (ASME), New York (2006).

[16] T. Utsonomiya, T. Sato, H. Matsukuma, K. Yago, Experimental validation for motion of a spar- type floating offshore wind turbine using 1/22.5 scale model, Proc. Int. Conf. on Ocean Offshore and Arctic Engineering, Am. Soc. of Mech. Eng. (ASME), New York (2009).

[17] G.R Tomasicchio, A.M. Avossa, L. Riefolo, F. Ricciardelli, E. Musci, F. D'Alessandro, D. Vicinanza, Dynamic modelling of a spar buoy wind turbine, Proc. 36th Int. Conf. on Ocean, Offshore and Arctic Engineering, Am. Soc. of Mech. Eng. (ASME), Trondheim, Norway (2017)

[18] P. Lomonaco, R. Guanche, C. Vidal, I.J. Losada, L. Migoya, Measuring and modelling the behaviour of floating slender bodies under wind and wave action, Proc. Int. Conf. Coastlab 10, Barcelona, 54 (2010).

[19] L. Wan, Z. Gao, T. Moan, Experimental and numerical study of hydrodynamic responses of a combined wind and wave energy converter concept in survival modes, Coastal Engineering 104 (2015), pp. 151-169.

[20] A. Jain, A.N. Robertson, J.M. Jonkman, A.J. Goupee, R.W. Kimball, A.H.P. Swift, FAST Code Verification of Scaling Laws for DeepCwind Floating Wind System Tests, 22nd Int. Offshore and Polar Eng. Conf. Rhodes, Greece, June 17–22, 2012.

[21] H. Shin, Model test of the OC3-Hywind floating offshore wind turbine, Proceedings of 21st ISOPE. Maui, Hawaii, USA June 19-24, 2011.

[22] R.A. Smith, W.T. Moon, W.T. Kao, Experiments on flow about a yawed circular cylinder, ASME Paper N. 72-FE-2 (1972).

[23] M.B. Bryndum, D.T. Tsahalis, V. Jacobsen, Hydrodynamic forces on pipelines: model tests, J. of Offshore Mechanics and Arctic Engineering 114(4) (1992), pp. 231-241.

[24] B. Brunone, G.R. Tomasicchio, Wave kinematics at steep slopes: second-order model, Journal of Waterway, Port, Coastal and Ocean Engineering 123-5 (1997), pp. 223-232.

[25] D. Matha, Model Development and Loads Analysis of an Offshore Wind Turbine on a Tension Leg Platform, with a Comparison to Other Floating Turbine Concepts., Technical Report NREL/SR-500-45891 (2009).

[26] J. Jonkman, S. Butterfield, W. Musial, G. Scott, Definition of a 5-MW Reference Wind Turbine for Offshore System Development., Technical Report NREL/TP-500-38060 (2009).

[27] O.M. Faltinsen, Sea loads on ships and offshore structures, Cambridge University Press (1990).

[28] S.A. Mavrakos, STATMOOR User's manual, Laboratory for Floating Stuctures and Mooring Systems, School of Naval Architecture and Marine Engineering, National Technical University of Athens (1992).

[29] P.D. Sclavounos, C. Tracy, S. Lee, Floating off-shore wind turbines: responses in a sea state, Pareto optimal designs and economic assessment, Proc. 27th Int. Conf. on Off-shore mechanics and arctic engineering, OMAE (2008).

[30] E.P.D. Mansard, E.R. Funke, The measurement of incident and reflected spectra using a least squares method. Proc. 17th Int. Conf. on Coastal Engineering, Sidney, Australia (1980), pp. 154-172.

[31] IEC 61400-1, Ed. 2, Wind Turbine Generator Systems, Part 1: Safety Requirements (1999).

[32] IEC 61400-3, Ed1, Wind turbines, Part 3: Design requirements for offshore wind turbines (2009). California at Berkeley, Fourth Edition, Prentice Hall (2012).

[33] J.R. Browning, J. Jonkman, A. Robertson, A.J. Goupee, Calibration and validation of a spar-type floating offshore wind turbine model using the FAST dynamic simulation tool, Journal of Physics: Conference Series 555-1 (2014) 012015.

[34] E.H. Vanmarcke, On the distribution of the first-passage time for normal stationary random processes, J. Appl. Mech. 42 (1975), p.215-220.

[35] A.G. Davenport, Note on the distribution of the largest value of a random function with application to gust loading, Proc. Inst. Civ. Eng. (1964), pp. 187–196.

[36] C. Braccesi, F. Cianetti, G. Lori, D. Pioli, A Frequency Method for Fatigue Life Estimation of Mechanical

Components under Bimodal Random Stress Process, SDHM Structural Durability and Health Monitoring 1-4 (2005), pp. 277-290.

[37] P. Folgueras, S. Solari, M. Mier-Torrecilla, M. Doblaré, M.A. Losada, The extended Davenport peak factor as an extreme-value estimation method for linear combinations of correlated non-Gaussian random variables, J. Wind Eng. Ind. Aerodyn. 157 (2016), pp. 125–139.